Orthorhombic-Cubic Phase Transition in Rb2CoSi5O12 Leucite Analogue

BELL, Anthony Martin Thomas <http://orcid.org/0000-0001-5038-5621>

minerals

MDPI

Article

Orthorhombic-Cubic Phase Transition in $Rb_2CoSi_5O_{12}$ Leucite Analogue

Anthony Martin Thomas Bell

Materials and Engineering Research Institute (MERI), City Campus, Sheffield Hallam University, Howard Street, Sheffield S1 1WB, UK; anthony.bell@shu.ac.uk; Tel.: +44-1142253401

Abstract: An $Rb_2CoSi_5O_{12}$ leucite analogue has been synthesized. An ambient temperature X-ray powder diffraction study shows that this analogue has the *Pbca* orthorhombic structure of $Cs_2CdSi_5O_{12}$. A high temperature X-ray powder diffraction study on this analogue shows a *Pbca* orthorhombic to $Pa\bar{3}$ cubic phase transition at 457 K. The $Rb_2CoSi_5O_{12}$ unit cell volume initially *decreases* with increasing temperature on passing through this phase transition.

Keywords: X-ray powder diffraction; minerals; phase transitions; leucite silicate framework structures; Rietveld refinement

1. Introduction

Synthetic analogues of the silicate framework minerals leucite $KAlSi_2O_6$ [1] and pollucite $CsAlSi_2O_6$ [2] can be prepared with the general formulae **AB**Si_2O_6 and $\mathbf{A_2C}Si_5O_{12}$. **A** is an alkali metal cation (K, Rb, Cs), **B** is a trivalent cation (Al, B, Fe^{3+}, Ga) and **C** is a divalent cation (Be, Mg, Mn, Fe^{2+}, Co, Ni, Cu, Zn, Cd). These structures have tetrahedrally coordinated silicate frameworks with **B** or **C** cations partially substituting for Si on the tetrahedrally coordinated silicon sites (T-sites). **A** cations sit in the extra framework channels; these **A** cations can be removed by ion exchange which makes them of technological interest as possible storage media for radioactive Cs from nuclear waste [3].

Leucite analogues with high symmetry structures such as $I4_1/a$ tetragonal $KGaSi_2O_6$ [4] and *Ia*-3*d* cubic $Rb_2ZnSi_5O_{12}$ [5] have **B** and **C** cations disordered over the T-sites. However, lower symmetry leucite structures are known where **C** cations are ordered onto separate T-sites. The $P2_1/c$ monoclinic $K_2MgSi_5O_{12}$ [6] structure has twelve crystallographically distinct and fully ordered T-sites, ten of these are fully occupied by Si and two are fully occupied by Mg. Three more $K_2\mathbf{C}Si_5O_{12}$ (**C** = Fe^{2+}, Co, Zn) structures [7] are known which are isostructural with $P2_1/c$ monoclinic $K_2MgSi_5O_{12}$ and have fully ordered T-sites. The *Pbca* orthorhombic structure of $Cs_2CdSi_5O_{12}$ [8] has six crystallographically distinct and fully ordered T-sites, five of these are fully occupied by Si and one is fully occupied by Cd. Five more structures with the general formula $Cs_2\mathbf{C}Si_5O_{12}$ (**C** = Mg, Mn, Co, Cu, Zn) [9–11], four structures with the general formula $Rb_2\mathbf{C}Si_5O_{12}$ (**C** = Mg, Mn, Ni, Cd) [9,10,12] and three structures with the general formula $RbCs\mathbf{C}Si_5O_{12}$ (**C** = Mg, Ni, Cd) [13] are all isostructural with the fully T-site cation ordered structure of $Cs_2CdSi_5O_{12}$. However, Nuclear Magnetic Resonance spectroscopy [14] and high-resolution synchrotron X-ray powder diffraction [10] studies on $Cs_2ZnSi_5O_{12}$ described a *Pbca* structure where Zn is partially disordered over two of the six T-sites.

High temperature neutron and X-ray powder diffraction studies on $KAlSi_2O_6$, $RbAlSi_2O_6$ and $KFe^{3+}Si_2O_6$ [15] and $KGaSi_2O_6$ [4] showed first-order phase transitions from $I4_1/a$ to *Ia*-3*d* (isostructural with pollucite $CsAlSi_2O_6$). High temperature X-ray powder diffraction studies on $K_2MgSi_5O_{12}$ [16] and $K_2ZnSi_5O_{12}$ [17] showed first-order phase transitions from $P2_1/c$ to *Pbca* (isostructural with $Cs_2CdSi_5O_{12}$.)

Citation: Bell, A.M.T. Orthorhombic-Cubic Phase Transition in $Rb_2CoSi_5O_{12}$ Leucite Analogue. *Minerals* **2023**, *13*, 210. https://doi.org/10.3390/min13020210

Academic Editors: Oxana Karimova and Sergey V. Krivovichev

Received: 8 December 2022
Revised: 27 January 2023
Accepted: 30 January 2023
Published: 31 January 2023

A high temperature study from 295 to 1173 K [18] has also been done on three $Cs_2\mathbf{C}Si_5O_{12}$ (**C** = Cu, Cd, Zn) leucite analogues using lower resolution synchrotron X-ray powder diffraction. For $Cs_2ZnSi_5O_{12}$, the ambient temperature crystal structure shows (unlike for the high-resolution synchrotron X-ray powder diffraction study) that the *Pbca* structure is also isostructural with $Cs_2CdSi_5O_{12}$ with complete T-site cation ordering. However, the sample with **C** = Zn shows evidence for a transition to a previously unknown $Pa\overline{3}$ cubic structure, with some T-site cation disorder, at 566 K, on heating. This transition is reversible on cooling to 633 K.

$Rb_2\mathbf{C}Si_5O_{12}$ leucite structures are known where **C** = Cd, Ni, Mg, Mn and Zn [5,7,9,10,12] as is the structure of $Cs_2CoSi_5O_{12}$ [9]. A cubic lattice parameter of 13.4(1)Å for $Rb_2CoSi_5O_{12}$ has been reported [19] but there is no published crystal structure for this leucite analogue. Therefore, a sample of $Rb_2CoSi_5O_{12}$ leucite analogue has been synthesized. An ambient temperature X-ray powder diffraction study on this analogue has been undertaken to determine the crystal structure for $Rb_2CoSi_5O_{12}$. A high temperature X-ray powder diffraction study has also been done to look for any phase transitions.

2. Materials and Methods

A sample of $Rb_2CoSi_5O_{12}$ was synthesized from a stoichiometric mixture of Rb_2CO_3 (Alfa Aesar, Heysham, United Kingdom, 99.5%); CoO (Sigma-Aldrich, St. Louis, MO, USA, 99.98%) and SiO_2 (Better Equipped purified white silica sand, Nantwich, United Kingdom). The mixture was then heated overnight at 873 K to decompose the carbonates and melted in a platinum crucible at 1673 K for 1.5 h before quenching to form a glass. The $Rb_2CoSi_5O_{12}$ glass was then dry crystallized at ambient pressure and 1393 K for 5 days. These were the same sample preparation conditions as were used to synthesise $Cs_2CoSi_5O_{12}$ leucite analogue [9].

This sample was then mounted on a low-background silicon wafer with a drop of acetone. Ambient temperature X-ray powder diffraction was then collected on this sample using a PANalytical Empyrean X-ray powder diffractometer (PANalytical, Almelo, Netherlands). Data were collected using Co*K*a X-rays over the range from 12 to 100 °2θ, the scan time was 19 h.

This $Rb_2CoSi_5O_{12}$ sample was then loaded into a platinum flat plate sample holder which was loaded into an Anton HTK1200N high temperature stage mounted on a PANalytical X'Pert MPD X-ray powder diffractometer (PANalytical, Almelo, Netherlands). Data were collected using Cu*K*a X-rays over the range from 10 to 80 °2θ. Scans were done at ambient temperature (scan time 30 min) and then in 50 K increments (scan time 2.5 h) from 323 to 1373 K. A second series of high temperature scans were done $Rb_2CoSi_5O_{12}$ on using the HTK1200N over the range from 10 to 80 °2θ. Scans were done in 10 K increments from 423 to 523 K, the scan time at each temperature was 8 h. A final scan on cooling to ambient temperature was also measured over the range from 10 to 80 °2θ, the scan time was 30 min.

High temperature X-ray powder diffraction data were also collected on a sample of MgO (99.99%, Acros Organics, New Jersey, USA) to calibrate the temperature of the HTK1200N. This was loaded into a platinum flat plate sample holder which was loaded onto the same Anton HTK1200N high temperature stage. Data were collected over the range from 33 to 111 °2θ, the scan time at each temperature was 10 min. Scans were done at ambient temperature and then in 50 K increments from 323 to 1473 K.

Thermogravimetric Analysis (TGA) and Differential Scanning Calorimetry (DSC) were collected on a sample of $Rb_2CoSi_5O_{12}$ from ambient temperature to 1673 K. Data were collected in a TA Instruments SDT 650 simultaneous TGA/DSC (New Castle, DE, USA), under a flow of compressed air. The instrument was suitably calibrated, an empty alumina crucible was used for the sample holder and reference sample, with no background corrections.

3. Results

3.1. Ambient Temperature X-ray Powder Diffraction

Analysis of the ambient temperature powder diffraction data collected on $Rb_2CoSi_5O_{12}$ showed that the observed powder diffraction data were a close match to the Powder Diffraction File (http://www.icdd.com/ (accessed on 5 April 2022)) pattern 70-0007 for $Rb_2NiSi_5O_{12}$. Therefore, the *Pbca* crystal structure for $Rb_2NiSi_5O_{12}$ [12], with Co replacing Ni on one of the T-sites, was used as a starting model for Rietveld refinement [20] using GSAS-II [21]. Si-O and Co-O distances for T-sites were restrained to those in the crystal structure for $Cs_2CoSi_5O_{12}$ [9].

Figure 1 shows the Rietveld difference plot for ambient temperature $Rb_2CoSi_5O_{12}$. Note that the X-ray powder diffraction data collected for this figure were collected in automatic divergence slit mode. These data were converted to fixed slit mode for Rietveld refinement, hence the very high background at low 2θ angles. Figure 2 shows a VESTA [22] crystal structure plot for the refined ambient temperature *Pbca* crystal structure of $Rb_2CoSi_5O_{12}$. Table 1 shows the refined ambient temperature coordinates for $Rb_2CoSi_5O_{12}$. Tables 2 and 3 show the interatomic distances and angles for ambient temperature $Rb_2CoSi_5O_{12}$.

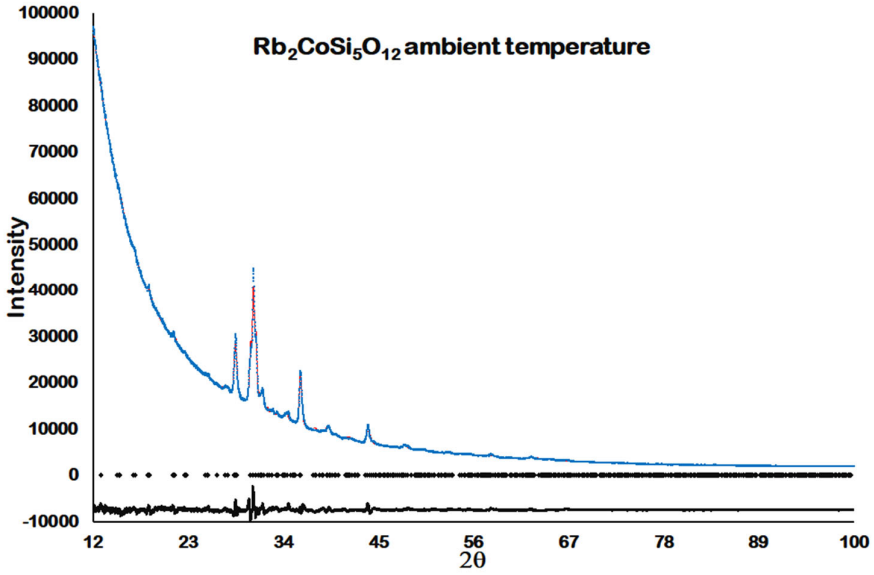

Figure 1. Ambient temperature Rietveld difference plot for $Rb_2CoSi_5O_{12}$. Blue dots show observed data, red line shows calculated data, black line shows difference plot and black diamonds show positions of Bragg reflections.

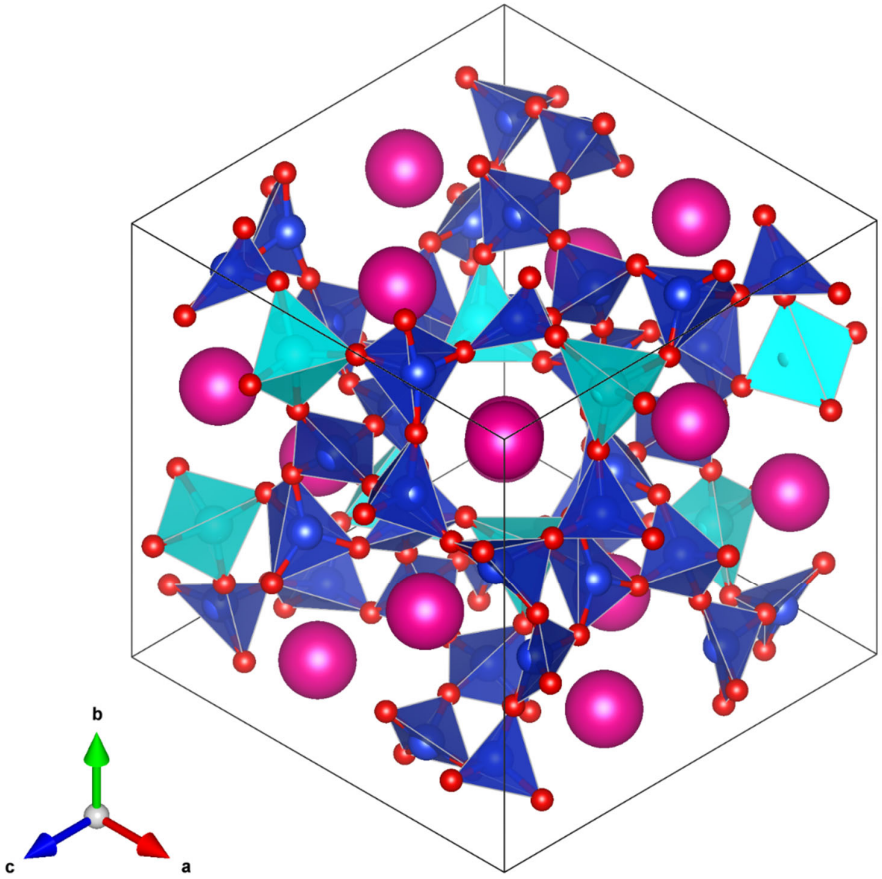

Figure 2. VESTA plot showing the ambient temperature *Pbca* orthorhombic crystal structure of $Rb_2CoSi_5O_{12}$. Pink spheres represent Rb^+ cations, red spheres represent O^{2-} anions, dark blue tetrahedra represent SiO_4 units and light blue tetrahedra represent CoO_4 units.

Table 1. Refined atomic coordinates for ambient temperature $Rb_2CoSi_5O_{12}$.

$Rb_2CoSi_5O_{12}$ *Pbca* Orthorhombic. All Sites Fully Occupied and all Atoms on 8*c* Wyckoff Position.				
	a (Å)	*b* (Å)	*c* (Å)	*V* (Å^3)
	13.370(4)	13.639(4)	13.497(4)	2461.4(20)
Atom	*x*	*y*	*z*	*Uiso*
Rb1	0.1455(9)	0.1306(11)	0.1371(17)	0.270(6)
Rb2	0.3751(12)	0.3606(11)	0.3787(17)	0.270(6)
Co1	0.3468(22)	0.8405(22)	0.9184(16)	0.203(14)
Si1	0.1223(29)	0.628(3)	0.610(3)	0.117(7)
Si2	0.6105(30)	0.1033(25)	0.6364(30)	0.117(7)
Si3	0.6625(27)	0.5965(31)	0.115(3)	0.117(7)
Si4	0.9115(24)	0.355(3)	0.8258(31)	0.117(7)
Si5	0.8438(29)	0.9494(27)	0.363(4)	0.117(7)
O1	0.4908(29)	0.418(3)	0.122(5)	0.036(5)
O2	0.1957(31)	0.4815(29)	0.380(5)	0.036(5)
O3	0.3650(30)	0.1469(25)	0.490(3)	0.036(5)
O4	0.7292(24)	0.4557(22)	0.615(4)	0.036(5)
O5	0.6223(26)	0.757(4)	0.356(4)	0.036(5)
O6	0.380(3)	0.594(3)	0.7432(29)	0.036(5)
O7	0.9792(31)	0.8219(30)	0.635(4)	0.036(5)

O8	0.5673(27)	0.968(3)	0.860(5)	0.036(5)
O9	0.885(3)	0.6312(31)	0.9438(19)	0.036(5)
O10	0.2217(30)	0.9414(30)	0.1311(31)	0.036(5)
O11	0.1722(23)	0.2036(27)	0.886(3)	0.036(5)
O12	0.9090(31)	0.142(4)	0.2032(31)	0.036(5)

Table 2. Refined interatomic distances (Å) for ambient temperature $Rb_2CoSi_5O_{12}$.

Rb1	O1	3.44(5)	Co1	O4	1.926(6)
Rb1	O2	3.85(6)	Co1	O7	1.925(6)
Rb1	O3	4.13(4)	Co1	O9	1.966(6)
Rb1	O4	3.72(6)	Co1	O11	1.935(6)
Rb1	O5	3.55(4)	Si1	O1	1.642(6)
Rb1	O6	4.04(5)	Si1	O3	1.643(6)
Rb1	O7	3.56(6)	Si1	O5	1.639(6)
Rb1	O8	4.07(4)	Si1	O10	1.654(6)
Rb1	O9	3.45(4)	Si2	O1	1.638(6)
Rb1	O10	2.78(4)	Si2	O2	1.639(6)
Rb1	O11	3.55(6)	Si2	O6	1.635(6)
Rb1	O12	3.29(5)	Si2	O11	1.625(6)
Rb2	O1	3.88(6)	Si3	O2	1.631(6)
Rb2	O2	2.91(5)	Si3	O3	1.627(6)
Rb2	O3	3.28(4)	Si3	O4	1.614(6)
Rb2	O4	2.87(3)	Si3	O12	1.645(6)
Rb2	O5	3.46(5)	Si4	O5	1.642(6)
Rb2	O6	3.72(5)	Si4	O7	1.620(6)
Rb2	O7	4.00(6)	Si4	O8	1.631(6)
Rb2	O8	3.49(4)	Si4	O12	1.656(6)
Rb2	O9	3.33(5)	Si5	O6	1.627(6)
Rb2	O10	3.75(5)	Si5	O8	1.641(6)
Rb2	O11	2.85(4)	Si5	O9	1.640(6)
Rb2	O12	3.21(6)	Si5	O10	1.639(6)
mean Rb1-O		3.62	mean Co-O		1.938
stdev Rb1-O		0.38	mean Si-O		1.636
mean Rb2-O		3.40			
stdev Rb2-O		0.39			
mean Rb-O		3.51			
stdev Rb-O		0.40			

Table 3. Refined interatomic angles (°) for ambient temperature $Rb_2CoSi_5O_{12}$.

O4	Co1	O7	120.4(26)	Si1	O1	Si2	148(4)
O4	Co1	O9	101.3(27)	Si2	O2	Si3	120(4)
O7	Co1	O9	98.1(20)	Si1	O3	Si3	145(3)
O4	Co1	O11	131.7(23)	Co1	O4	Si3	96.6(26)
O7	Co1	O11	84.8(24)	Si1	O5	Si4	164(3)
O9	Co1	O11	116.0(21)	Si2	O6	Si5	158(4)
O1	Si1	O3	104.5(30)	Co1	O7	Si4	156(3)
O1	Si1	O5	109(4)	Si4	O8	Si5	122.2(28)
O3	Si1	O5	97(4)	Co1	O9	Si5	132(4)
O1	Si1	O10	121(4)	Si1	O10	Si5	148(4)
O3	Si1	O10	100.3(31)	Co1	O11	Si2	141.9(28)

O5	Si1	O10	120(4)	Si3	O12	Si4	138(3)
O1	Si2	O2	123(3)	mean Si-O-Si			142.9
O1	Si2	O6	100(4)	mean Co-O-Si			131.6
O2	Si2	O6	91(3)				
O1	Si2	O11	128(3)				
O2	Si2	O11	102.5(30)				
O6	Si2	O11	102(3)				
O2	Si3	O3	120(4)				
O2	Si3	O4	48.0(18)				
O3	Si3	O4	113(4)				
O2	Si3	O12	120(5)				
O3	Si3	O12	109.8(22)				
O4	Si3	O12	134(4)				
O5	Si4	O7	84.8(25)				
O5	Si4	O8	149(4)				
O7	Si4	O8	91(3)				
O5	Si4	O12	105(4)				
O7	Si4	O12	110.7(30)				
O8	Si4	O12	105(4)				
O6	Si5	O8	90.4(28)				
O6	Si5	O9	104.1(26)				
O8	Si5	O9	104(4)				
O6	Si5	O10	108(4)				
O8	Si5	O10	140.3(29)				
O9	Si5	O10	105(3)				
mean O-Co-O			108.7				
mean O-Si-O			108.0				

3.2. High Temperature X-ray Powder Diffraction

3.2.1. First High Temperature Scans

The first series of high temperature scans were done in 50 K increments from 323 to 1373 K. The strongest Bragg reflections in the Pbca orthorhombic powder diffraction patterns for $Rb_2CoSi_5O_{12}$ were three closely overlapped 004, 040 and 400 Bragg reflections. As the temperature increases, these three reflections merge to form a single peak by 473 K, suggesting a phase transition from orthorhombic to cubic. This single peak is retained to 1123 K. However, at higher temperatures extra peaks appear in the powder diffraction pattern before all the $Rb_2CoSi_5O_{12}$ peaks disappear at 1323 K; it was not possible to identify any phase(s) causing these extra peaks as the $Rb_2CoSi_5O_{12}$ started to decompose. When the sample was removed from the high temperature stage, on cooling to ambient temperature, the sample appeared to have partially melted. Figure 3 shows all the powder diffraction data collected on heating 298–1123 K. Figure 4 shows how the closely overlapped 004, 040 and 400 Bragg reflections merge to a single peak on heating 298–1123 K.

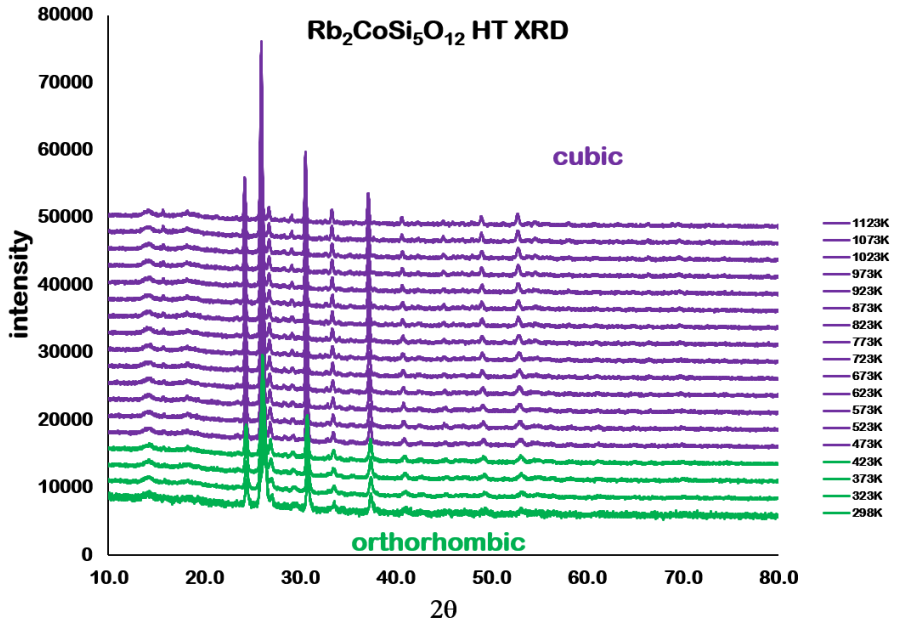

Figure 3. Plot showing XRD data for $Rb_2CoSi_5O_{12}$ 10–80 °2θ over the temperature range 298–1123 K. *Pbca* orthorhombic data are shown in green and $Pa\bar{3}$ cubic are shown in purple.

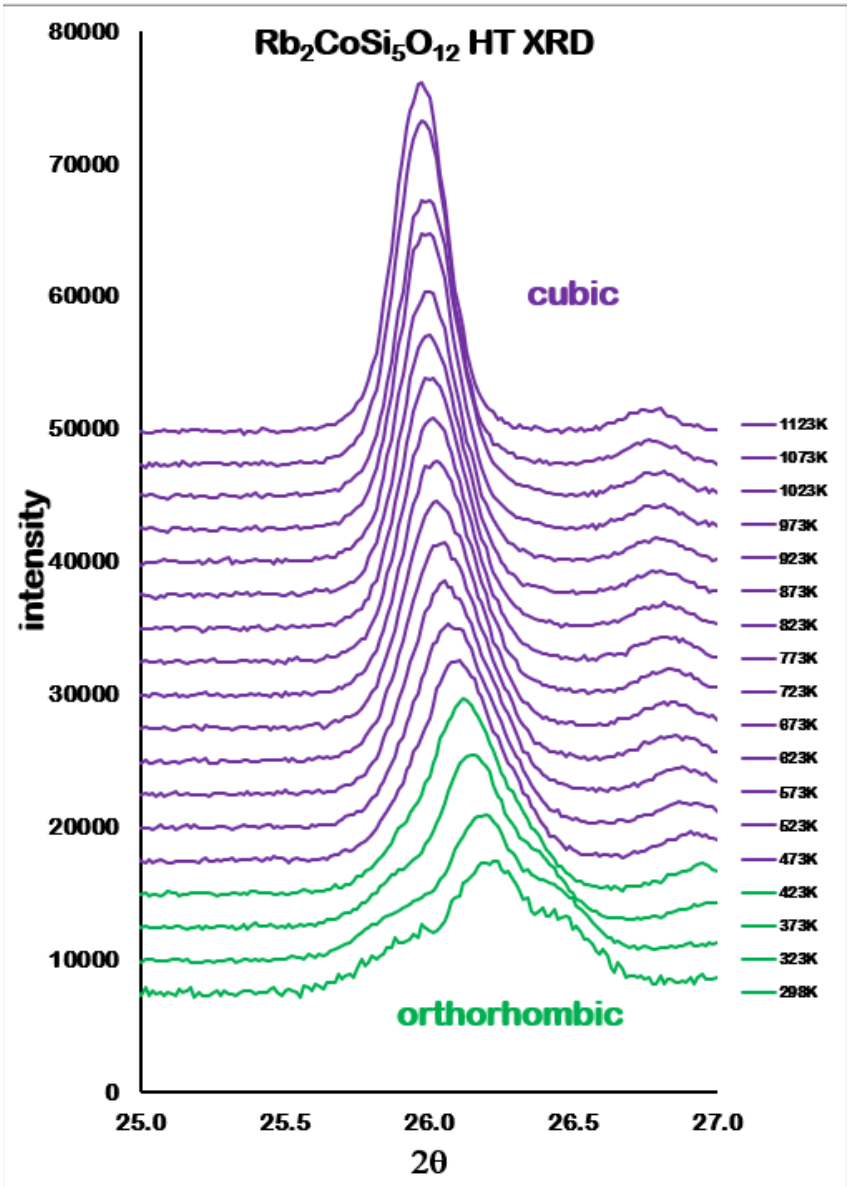

Figure 4. Plot showing XRD data for $Rb_2CoSi_5O_{12}$ 25–27 °2θ over the temperature range 298–1123 K. This shows how three closely overlapped 004, 040 and 400 *Pbca* orthorhombic Bragg reflections (green) merge to form a single $Pa\bar{3}$ cubic 400 Bragg reflection (purple) on heating.

3.2.2. Second High Temperature Scans

The second series of high temperature scans were done in 10 K increments from 423 to 523 K to determine more precisely the orthorhombic to cubic transition temperature. Some Bragg reflections from the platinum sample holder were also observed in the powder diffraction data from the second series of high temperature scans, these platinum peaks were excluded from the Rietveld refinements. Figure 5 shows all the powder diffraction data collected. Figure 6 shows how the closely overlapped 004, 040 and 400 Bragg reflections merge to a single peak on heating 423–523 K.

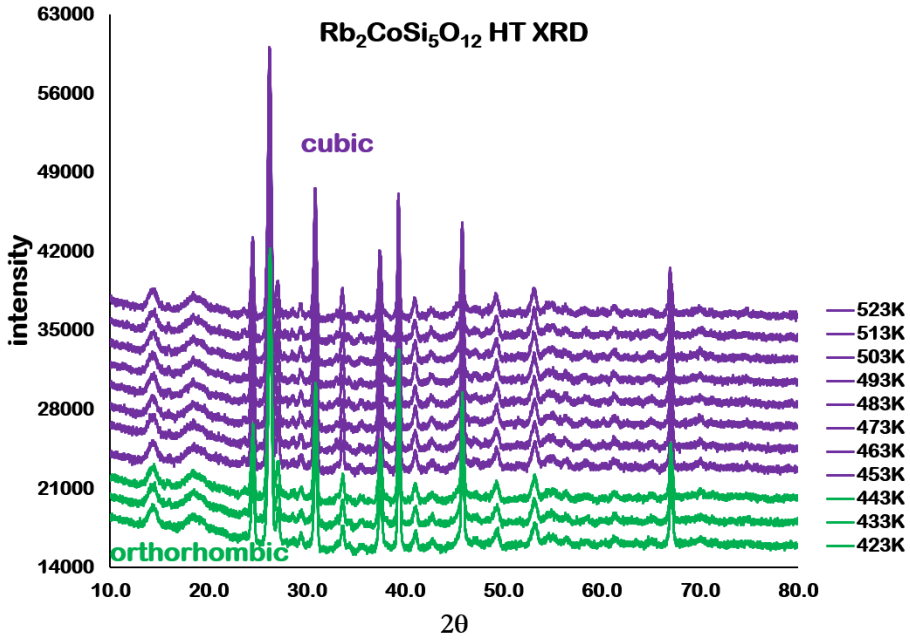

Figure 5. Plot showing XRD data for $Rb_2CoSi_5O_{12}$ 25–27 °2θ over the temperature range 423–523 K. *Pbca* orthorhombic data are shown in green and $Pa\bar{3}$ cubic are shown in purple. Broad peaks at approximately 14 and 18 °2θ are due to the window material of the HTK1200N high temperature stage. Sharp peaks at approximately 39, 46 and 69 °2θ are due to the platinum sample holder.

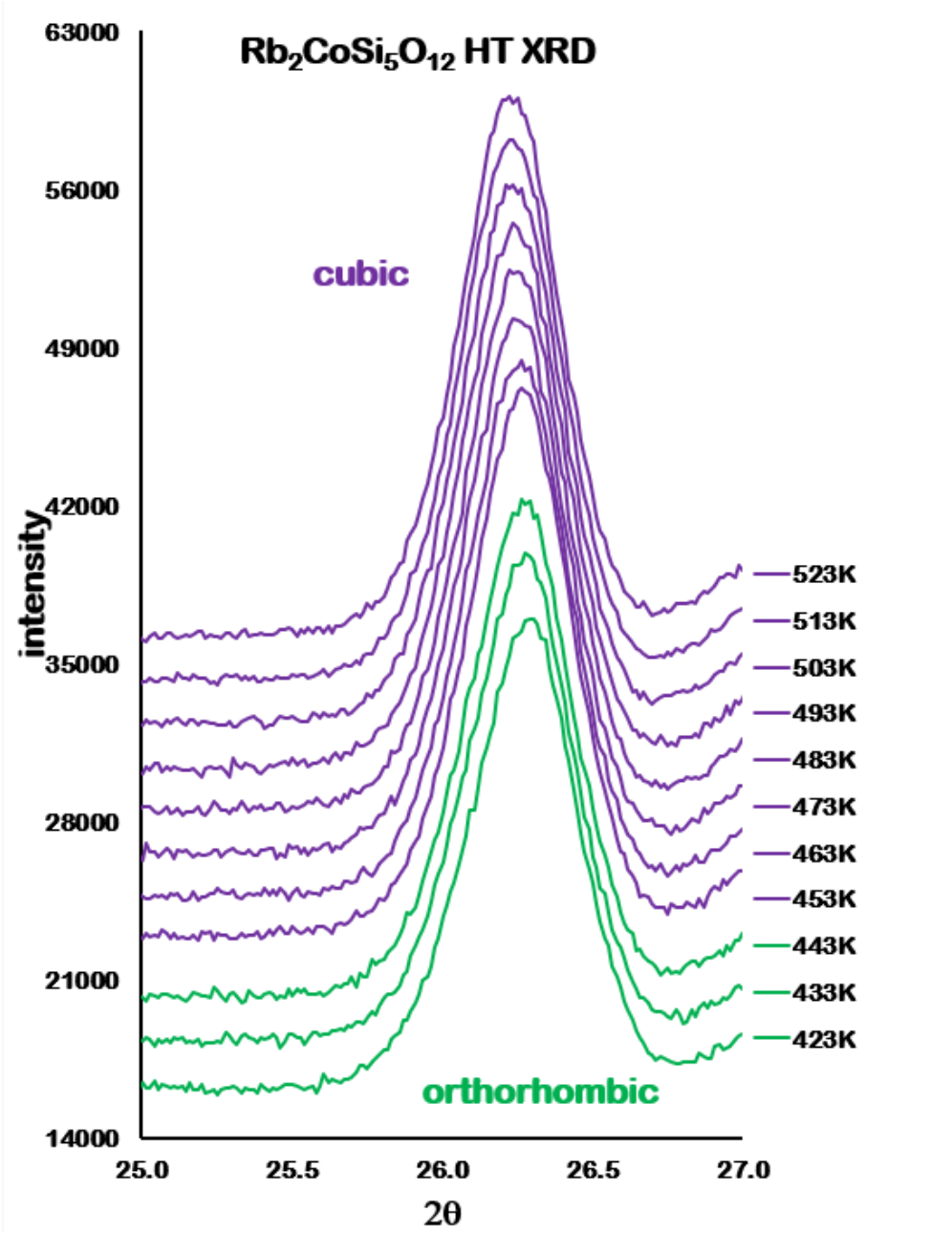

Figure 6. Plot showing XRD data for $Rb_2CoSi_5O_{12}$ 25–27 °2θ over the temperature range 423–523 K. This shows how three closely overlapped 004, 040 and 400 *Pbca* orthorhombic Bragg reflections (green) merge to form a single $Pa\bar{3}$ cubic 400 Bragg reflection (purple) on heating.

3.2.3. MgO Temperature Calibration Scans

The $Fm\bar{3}m$ cubic structure of MgO [23] was used as a starting model for Rietveld refinements of the MgO crystal structure over the whole temperature range. The refined MgO lattice parameters determined at each temperature and thermal expansion parameters for MgO [24] were then used to calibrate the temperature of the HTK1200N. The second high temperature scan data, collected in 10 K increments from 423 to 523 K, were calibrated by interpolating between the calibrated temperatures from the MgO data collected at 423, 473 and 523 K.

3.2.4. TGA/DSC Analyses

No significant changes were detected by TGA/DSC on heating $Rb_2CoSi_5O_{12}$ around the phase transition temperature.

3.3. Rietveld Refinement Data Analysis

All high temperature powder diffraction data from the two series of scans up to 443 K could be refined using the *Pbca* orthorhombic ambient temperature structure for $Rb_2CoSi_5O_{12}$ as a starting model. All high temperature powder diffraction data from the two series of scans from 453 K to 1123 K could be refined using a $Pa\overline{3}$ cubic structure isostructural with the high temperature crystal structure for $Cs_2ZnSi_5O_{12}$ [18]. The ambient temperature structure for $Rb_2CoSi_5O_{12}$ after heating reverts to Pbca orthorhombic.

Table 4 shows how the $Rb_2CoSi_5O_{12}$ lattice parameters vary with MgO calibrated temperature. Figures 7 and 8 show how the lattice parameters and unit cell volumes vary with MgO calibrated temperature.

To study the changes in the $Rb_2CoSi_5O_{12}$ structure with temperature the variance of the intratetrahedral O-T-O (T = Co and Si) angles (compared with the ideal tetrahedral angle of 109.5°) in the 6 *Pbca* orthorhombic T-sites and 2 $Pa\overline{3}$ cubic T-sites have been determined using the following equation [25]

$$\theta\sigma_{(tet)}^2 = \sum_{i=1}^{n} (\theta_i - 109.5)^2/(n-1)$$

where n is the number of different O-T-O angles (n = 6) and θ is the O-T-O angle in each TO_4 unit. Figure 9 shows how these T-site distortion parameters vary with temperature for the structures of *Pbca* orthorhombic and $Pa\overline{3}$ cubic $Rb_2CoSi_5O_{12}$.

Figure 10 shows a VESTA [22] plot and Figure 11 shows the Rietveld difference plot for the 1133 K (MgO calibrated temperature) $Pa\overline{3}$ cubic structure of $Rb_2CoSi_5O_{12}$. Table 5 shows refined 1133 K (MgO calibrated temperature) coordinates for $Rb_2CoSi_5O_{12}$. Tables 6 and 7 show interatomic distances and angles for 1133 K (MgO calibrated temperature) $Rb_2CoSi_5O_{12}$.

Table 4. Variation of lattice parameters with calibrated temperatures for $Rb_2CoSi_5O_{12}$.

T (K)	T—MgO (K)	a(Å)	b(Å)	c(Å)	V(Å^3)
298	+	13.370(4)	13.639(4)	13.497(4)	2461.4(20)
298	++	13.444(13)	13.612(9)	13.457(16)	2463(5)
298	303	13.416(8)	13.620(8)	13.495(8)	2466(4)
323	324	13.427(4)	13.612(4)	13.508(4)	2469(2)
373	376	13.455(3)	13.587(3)	13.518(3)	2471(2)
423	427	13.492(3)	13.604(2)	13.507(3)	2479(1)
433	437	13.494(3)	13.603(2)	13.509(3)	2480(1)
443	447	13.496(3)	13.606(2)	13.516(3)	2482(1)
453	457	13.532(1)			2477.7(6)
463	467	13.533(1)			2478.4(6(
473	477	13.536(1)			2480.2(6)
483	487	13.541(1)			2482.8(5)
493	497	13.544(1)			2484.4(5)
503	507	13.5448(9)			2485.0(5)
513	517	13.5478(9)			2486.6(5)
523	528	13.5498(9)			2487.7(5)
573	581	13.5495(9)			2487.5(5)

623	632	13.5545(9)	2490.3(5)
673	684	13.5609(8)	2493.8(5)
723	736	13.5686(8)	2498.1(4)
773	785	13.5709(7)	2499.3(4)
823	835	13.5775(7)	2503.0(4)
873	883	13.5820(7)	2505.5(4)
923	935	13.5853(6)	2507.3(3)
973	986	13.5885(6)	2509.07(31)
1023	1036	13.5919(5(	2510.95(27)
1073	1084	13.5968(5)	2513.67(26)
1123	1133	13.6008(5)	2515.88(26)

+ = ambient temperature scan outside high temperature stage. ++ = ambient temperature scan in high temperature stage after heating.

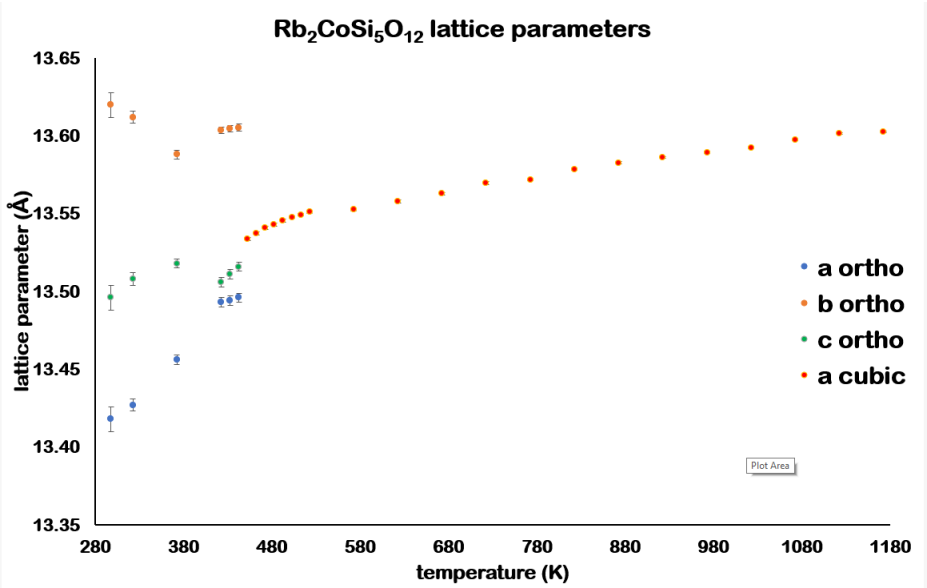

Figure 7. Variation of *Pbca* orthorhombic *a, b* and *c* lattice parameters and $Pa\bar{3}$ cubic *a* lattice parameter with calibrated temperatures for $Rb_2CoSi_5O_{12}$.

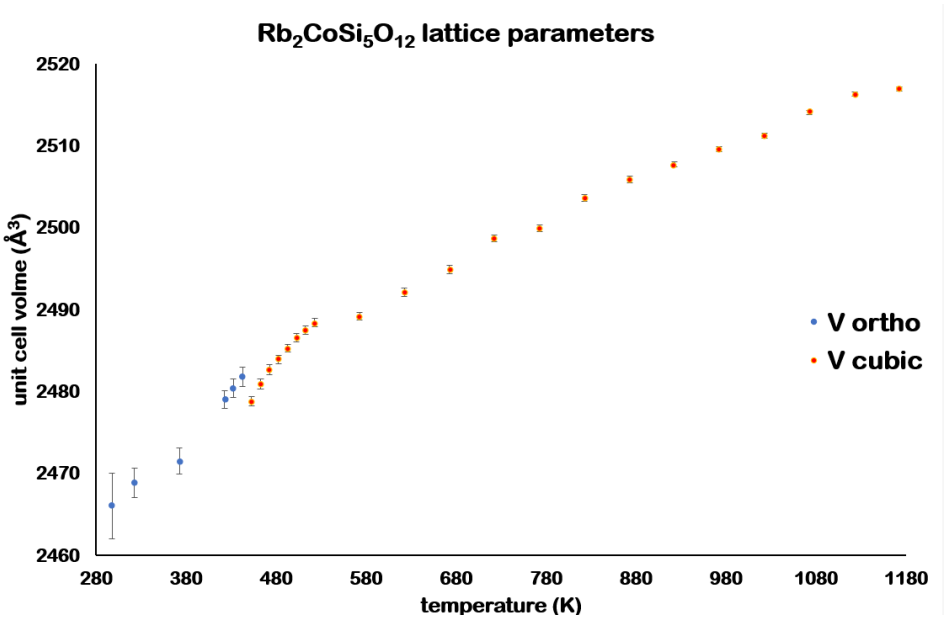

Figure 8. Variation of *Pbca* orthorhombic and $Pa\bar{3}$ cubic unit cell volumes with calibrated temperatures for $Rb_2CoSi_5O_{12}$.

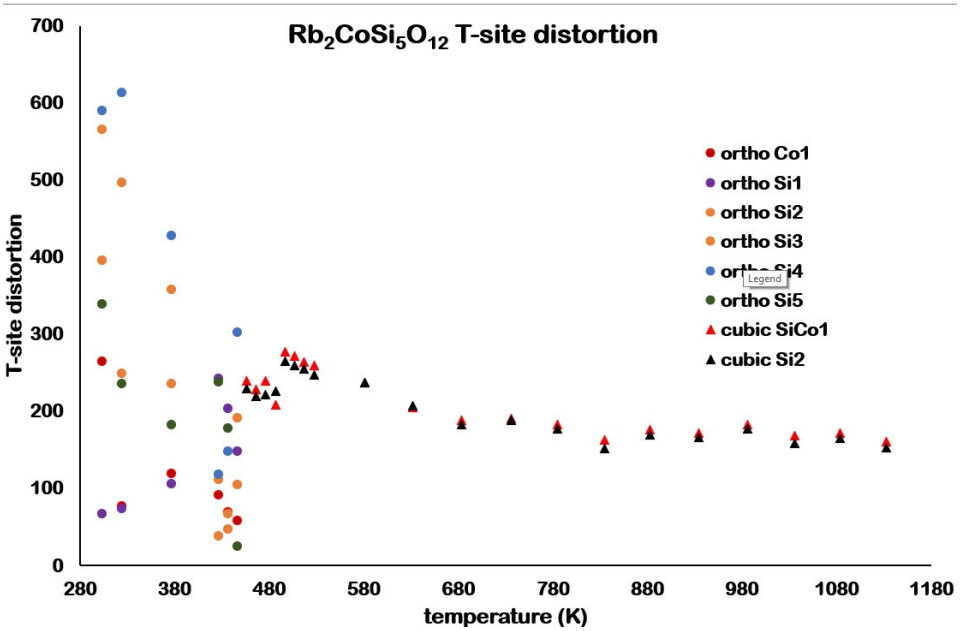

Figure 9. Variation of T-site distortion parameters with temperature showing how these parameters vary for the structures of *Pbca* orthorhombic and $Pa\bar{3}$ cubic $Rb_2CoSi_5O_{12}$.

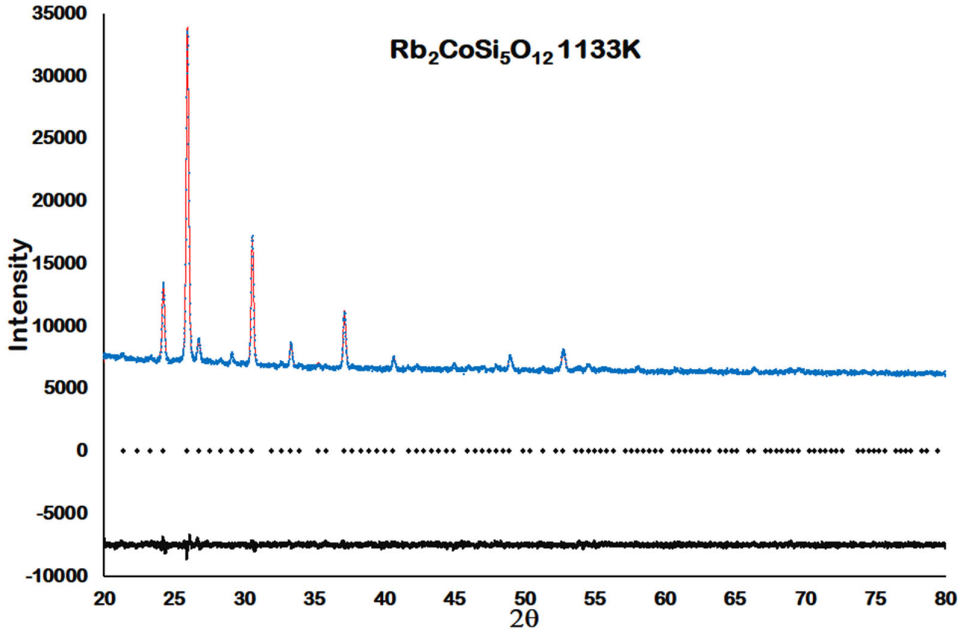

Figure 10. 1133 K (MgO calibrated temperature) Rietveld difference plot for $Rb_2CoSi_5O_{12}$. Blue dots show observed data, red line shows calculated data, black line shows difference plot and black diamonds show positions of Bragg reflections.

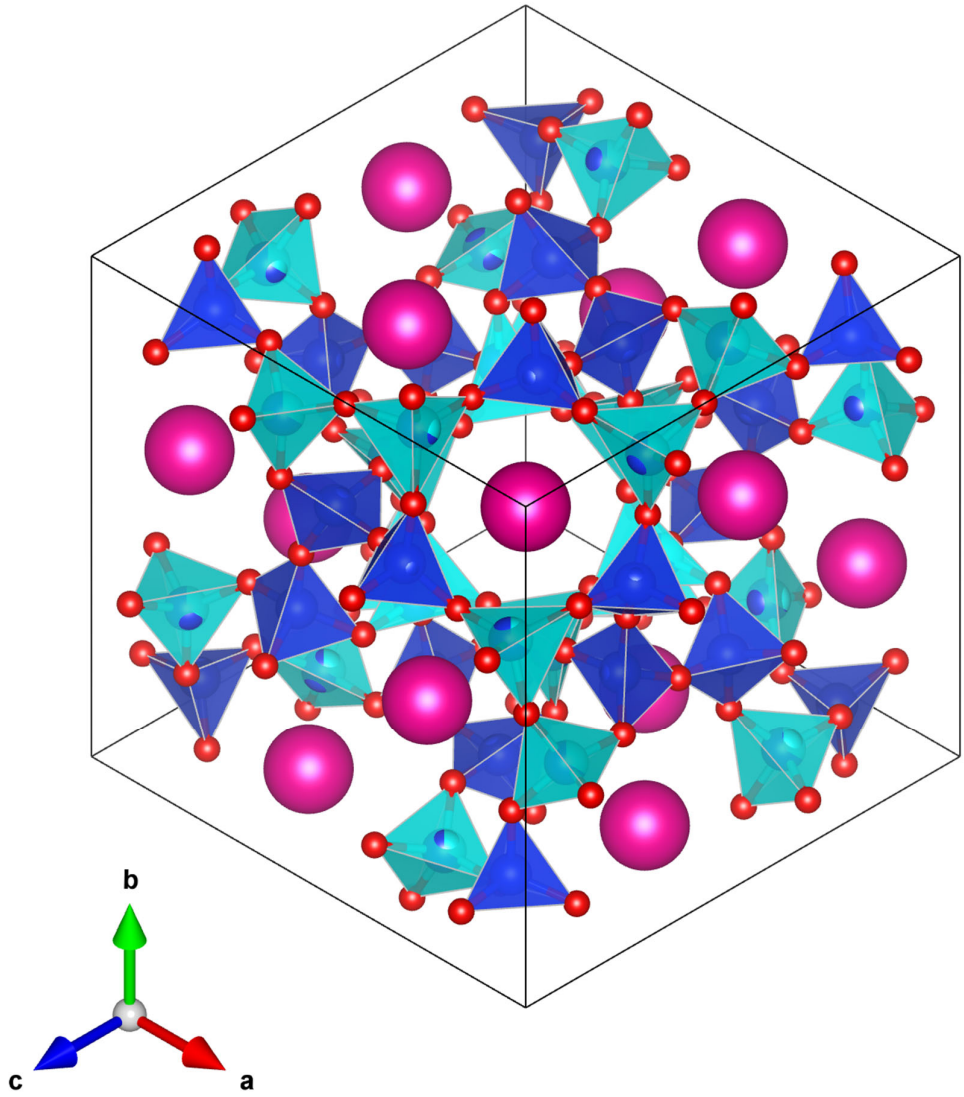

Figure 11. VESTA plot showing the 1133 K (MgO calibrated temperature) $Pa\bar{3}$ cubic crystal structure of $Rb_2CoSi_5O_{12}$. Pink spheres represent Rb^+ cations, red spheres represent O^{2-} anions, dark blue tetrahedra represent SiO_4 units and light blue tetrahedra represent $(Si_{2/3}Co_{1/3})O_4$ units.

Table 5. Refined atomic coordinates for 1133 K $Rb_2CoSi_5O_{12}$.

$Rb_2CoSi_5O_{12}$ $Pa\bar{3}$ Cubic						
a = 13.6008(5)Å		**V = 2515.88(26)Å^3**				
Atom	***x***	***y***	***Z***	**occ.**	***Uiso***	**Wyckoff**
Rb1	0.1363(5)	0.1363(5)	0.1363(5)	1.0000	0.142(6)	8*c*
Rb2	0.3871(6)	0.3871(6)	0.3871(6)	1.0000	0.124(5)	8*c*
Si1	0.36116(31)	0.82652(27)	0.9199(3)	0.6667	0.092(6)	24*d*
Co1	0.36116(31)	0.82652(27)	0.9199(3)	0.3333	0.092(6)	24*d*
Si2	0.1280(8)	0.6550(7)	0.5936(9)	1.0000	0.026(4)	24*d*
O1	0.4759(10)	0.3756(16)	0.1415(18)	1.0000	0.098(4)	24*d*
O2	0.1365(13)	0.7276(8)	0.1045(15)	1.0000	0.098(4)	24*d*
O3	0.9685(6)	0.8798(6)	0.6183(12)	1.0000	0.098(4)	24*d*
O4	0.6428(12)	0.20079(23)	0.5761(11)	1.0000	0.098(4)	24*d*

Table 6. Refined interatomic distances (Å) for 1133 K $Rb_2CoSi_5O_{12}$.

Rb1	O1	3.862(22)	Rb2	O1	3.555(25)	Si1/Co1	O2	1.7110(31)
Rb1	O1	3.862(24)	Rb2	O1	3.555(30)	Si1/Co1	O3	1.711(3)
Rb1	O1	3.862(23)	Rb2	O1	3.555(26)	Si1/Co1	O3	1.712(3)
Rb1	O2	3.358(18)	Rb2	O2	3.358(22)	Si1/Co1	O4	1.7117(30)
Rb1	O2	3.358(20)	Rb2	O2	3.358(26)	Si2	O1	1.610(3)
Rb1	O2	3.358(22)	Rb2	O2	3.358(21)	Si2	O1	1.613(3)
Rb1	O3	3.635(18)	Rb2	O3	3.358(9)	Si2	O2	1.608(3)
Rb1	O3	3.635(19)	Rb2	O3	3.358(12)	Si2	O4	1.606(3)
Rb1	O3	3.635(18)	Rb2	O3	3.358(9)	mean (Si1/Co1)-O		1.711
Rb1	O4	3.021(15)	Rb2	O4	3.567(17)	mean Si2-O		1.609
Rb1	O4	3.021(16)	Rb2	O4	3.567(17)			
Rb1	O4	3.021(15)	Rb2	O4	3.567(17)			
mean Rb1-O		3.469	mean Rb2-O		3.460			
stdev Rb1-O		0.328	stdev Rb2-O		0.106			
			mean Rb-O		3.464			
			stdev Rb-O		0.239			

Table 7. Refined interatomic angles (°) for 1133 K $Rb_2CoSi_5O_{12}$. T = Si or Co.

	O2	Si1/Co1	O3	103.5(7)
	O2	Si1/Co1	O3	105.2(11)
	O3	Si1/Co1	O3	87.5(8)
	O2	Si1/Co1	O4	122.7(9)
	O3	Si1/Co1	O4	117.4(6)
	O3	Si1/Co1	O4	114.5(9)
	O1	Si2	O1	110.3(18)
	O1	Si2	O2	106.4(13)
	O1	Si2	O2	101.9(9)
	O1	Si2	O4	101.6(9)
	O1	Si2	O4	110.9(14)
	O2	Si2	O4	125.5(11)
	Si2	O1	Si2	155.4(17)
	Si1/Co1	O2	Si2	136.0(12)
	Si1/Co1	O3	Si1/Co1	145.8(4)
	Si1/Co1	O4	Si2	125.6(9)
mean	O	Si1/Co1	O	108.5
mean	O	Si2	O	109.4
mean	O	T	O	109.0
mean	T	O	T	140.7

4. Discussion

All temperatures referred to in this section are now MgO calibrated temperatures.

Analysis of the high temperature X-ray powder diffraction data for $Rb_2CoSi_5O_{12}$ showed a first-order phase transition from *Pbca* orthorhombic to $Pa\overline{3}$ cubic at 457 K. However, Table 4 and Figures 7 and 8 show that the unit cell volume *decreases* with increasing temperature after the phase transition. The *Pbca* structure for $Rb_2CoSi_5O_{12}$ has the tetrahedrally coordinated Co and Si atoms ordered onto separate T-sites (1 Co and 5 Si sites). However, the $Pa\overline{3}$ structure for $Rb_2CoSi_5O_{12}$ has some partial T-site disorder. One T site is fully occupied by Si, the other T site is 2/3 occupied by Si and 1/3 occupied by Co. Figure 9 shows how the T-site distortions for $Rb_2CoSi_5O_{12}$ vary with temperature for the *Pbca* orthorhombic and $Pa\overline{3}$ cubic phases. There is a much wider spread of T-site

distortions for *Pbca* orthorhombic compared with $Pa\overline{3}$ cubic. A plot of the 447 K *Pbca* T-site ordered crystal structure (Figure 12) shows that the central channel (which contains different sized SiO_4 and CoO_4 tetrahedra) is much more distorted than the central channel of the partially T-site disordered 457 K $Pa\overline{3}$ structure (Figure 13). This agrees with the plot of T-site distortions shown in Figure 9. In the $Pa\overline{3}$ structure, there is a smaller size difference between the SiO_4 and $(Si_{2/3}Co_{1/3})O_4$ tetrahedra compared with the size difference between the *Pbca* SiO_4 and CoO_4 tetrahedra. The smaller size difference between the TO_4 (T = Si or Co) tetrahedra in the $Pa\overline{3}$ structure compared with the *Pbca* structure means that the $Pa\overline{3}$ structure is less distorted than the *Pbca* structure. This decrease in distortion of the crystal structure through the phase transition is why the central channel *contracts* through the phase transition. This is reflected in the decrease in unit cell volume.

Such a phase transition with a unit cell contraction has not been observed before in a leucite mineral analogue. However, similar transitions have been observed in other materials such as $BiNiO_3$ [26] and $Hf_{0.86}Ta_{0.14}Fe_2$ [27].

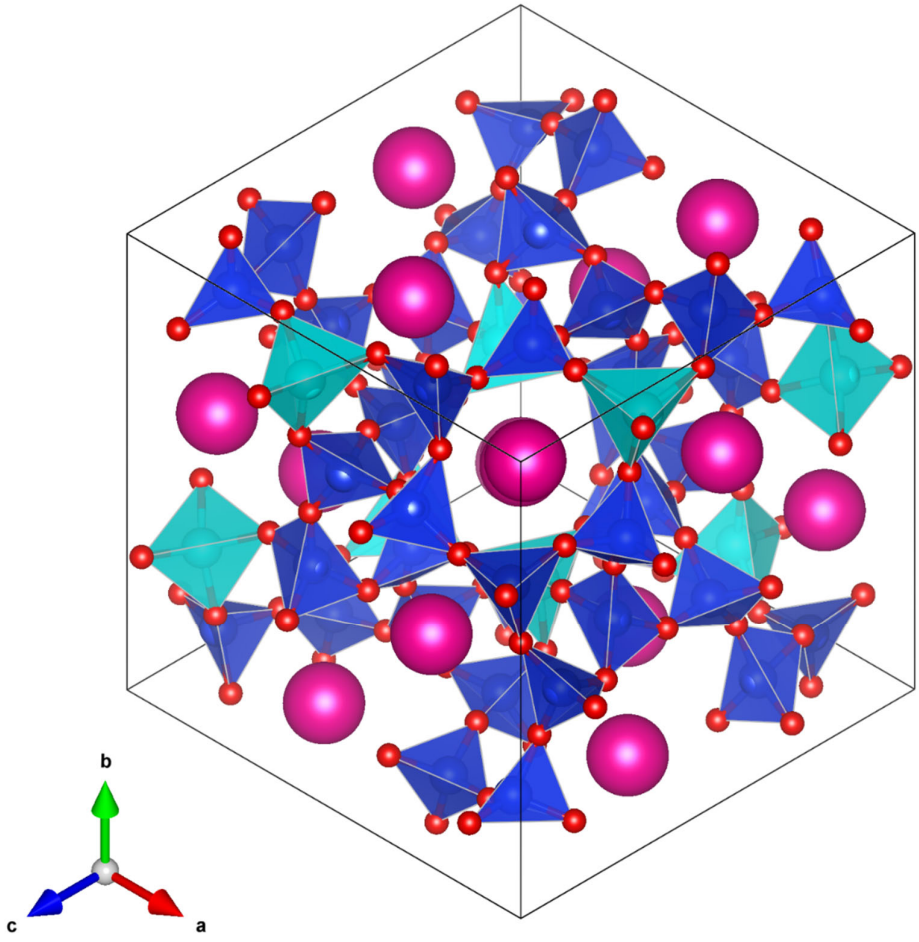

Figure 12. VESTA plot showing the 447 K (MgO calibrated temperature) *Pbca* orthorhombic crystal structure of $Rb_2CoSi_5O_{12}$. Pink spheres represent Rb^+ cations, red spheres represent O^{2-} anions, dark blue tetrahedra represent SiO_4 units and light blue tetrahedra represent CoO_4 units.

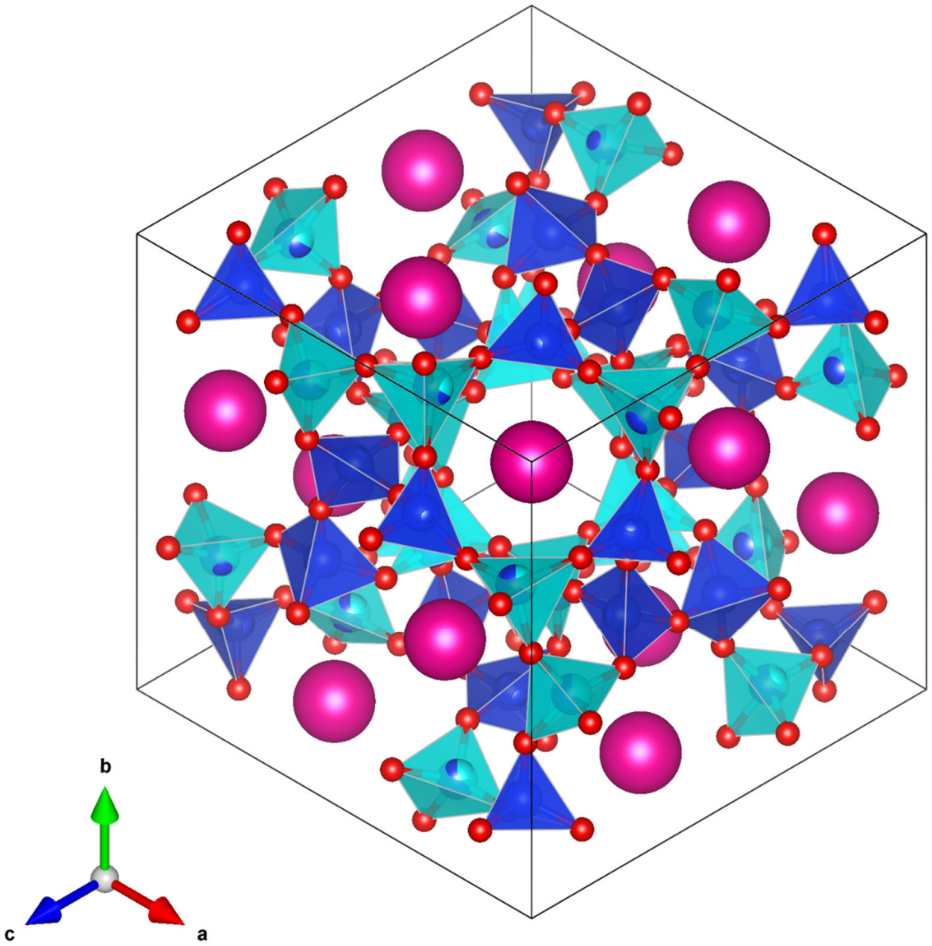

Figure 13. VESTA plot showing the 457 K (MgO calibrated temperature) $Pa\bar{3}$ cubic crystal structure of $Rb_2CoSi_5O_{12}$. Pink spheres represent Rb^+ cations, red spheres represent O^{2-} anions, dark blue tetrahedra represent SiO_4 units and light blue tetrahedra represent $(Si_{2/3}Co_{1/3})O_4$ units.

Thermal expansion due to the increase in temperature means that the cubic unit cell volume eventually becomes greater than the orthorhombic unit cell volume at 497 K, 40 K higher than the phase transition temperature. The $Pa\bar{3}$ cubic structure is retained up to 1133 K. Above this temperature the $Rb_2CoSi_5O_{12}$ sample starts to decompose before partially melting at 1323 K. Table 8 shows the thermal expansion coefficients (TEC) for the two $Rb_2CoSi_5O_{12}$ phases. TEC for other leucite phases are given as comparison. It can be seen that the TEC for $Rb_2CoSi_5O_{12}$ are in the same order of magnitude as those reported for other leucites.

The *Pbca* orthorhombic to $Pa\bar{3}$ cubic leucite phase transition was first observed in $Cs_2ZnSi_5O_{12}$ [18]. There was no unit cell contraction noticed through the phase transition in $Cs_2ZnSi_5O_{12}$ and this was assumed to be a second-order phase transition. However, the high temperature X-ray powder diffraction data for $Cs_2ZnSi_5O_{12}$ were collected every 30 K, a larger temperature increment than was used for $Rb_2CoSi_5O_{12}$. It would be interesting to repeat the high temperature XRD study on $Cs_2ZnSi_5O_{12}$ with a smaller temperature increment to see if a unit cell contraction could be observed for this phase transition.

Table 8. Thermal expansion coefficients (TEC) for leucite analogues.

Stoichiometry	SG	T (K)	Mean TEC (× 10^5 K^{-1})	Reference
$Rb_2CoSi_5O_{12}$	*Pbca*	303–447	4(1)	This work
$Rb_2CoSi_5O_{12}$	$Pa\bar{3}$	457–1133	4(2)	This work
$KGaSi_2O_6$	$I4_1/a$	298–873	5.2(4)	[4]
$KGaSi_2O_6$	*Ia*-3*d*	673–1473	8(2)	[4]
$K_2ZnSi_5O_{12}$	$P2_1/c$	773–843	10(1)	[17]
$K_2ZnSi_5O_{12}$	*Pbca*	868–973	6(3)	[17]
$Cs_2CdSi_5O_{12}$	*Pbca*	295–1173	1.8(4)	[18]
$Cs_2CuSi_5O_{12}$	*Pbca*	295–333	6(3)	[18]
$Cs_2CuSi_5O_{12}$	*Pbca*	333–1173	0.8(3)	[18]
$Cs_2ZnSi_5O_{12}$	*Pbca*	295–543	2(1)	[18]
$Cs_2ZnSi_5O_{12}$	$Pa\bar{3}$	573–1173	1.1(3)	[18]
$K_2MgSi_5O_{12}$	$P2_1/c$	293–647	5(1)	[16]
$K_2MgSi_5O_{12}$	*Pbca*	668–842	2(1)	[16]
$CsAlSi_2O_6$	$I4_1/a$	20–368	5.1(1.4)	[15]
$CsAlSi_2O_6$	*Ia*-3*d*	373–573	3.0(2.2)	[15]
$RbAlSi_2O_6$	$I4_1/a$	298–743	7.1(7)	[15]
$RbAlSi_2O_6$	*Ia*-3*d*	753–953	3(1)	[15]
$KAlSi_2O_6$	$I4_1/a$	4–923	5(1)	[15]
$KAlSi_2O_6$	*Ia*-3*d*	943–1023	4.1(6)	[15]
$KFeSi_2O_6$	$I4_1/a$	298–843	6.2(8)	[15]
$KFeSi_2O_6$	*Ia*-3*d*	853–1050	5(1)	[15]
Nat. leucite	$I4_1/a$	298–963	8.562	[28]
Nat. leucite	*Ia*-3*d*	963–1193	0.877	[28]
$KAlSi_2O_6$	$I4_1/a$	298–878	8.548	[28]
$KAlSi_2O_6$	$I4_1/a$	878–1093	6.323	[28]
$KAlSi_2O_6$	*Ia*-3*d*	1093–1193	0.921	[28]
$RbAlSi_2O_6$	$I4_1/a$	298–583	7.98	[28]
$RbAlSi_2O_6$	$I4_1/a$	583–793	4.653	[28]
$RbAlSi_2O_6$	*Ia*-3*d*	793–1193	1.215	[28]
$CsAlSi_2O_6$	*Ia*-3*d*	298–463	4.789	[28]

5. Conclusions

1. The ambient temperature crystal structure of the $Rb_2CoSi_5O_{12}$ leucite analogue has been determined as isostructural with the *Pbca* orthorhombic T-site ordered crystal structure of $Cs_2CdSi_5O_{12}$.
2. High temperature X-ray powder diffraction on $Rb_2CoSi_5O_{12}$ leucite analogue shows a *Pbca* orthorhombic to $Pa\bar{3}$ cubic phase transition at 457 K, like that reported for $Cs_2ZnSi_5O_{12}$. The decrease in the size difference between the TO_4 (T = Si and Co) units before and after this transition means that the central channel of the cubic leucite structure is less distorted than that for the orthorhombic structure. The decrease in structural distortion means that there is an initial unit cell contraction with increasing temperature after the phase transition.
3. The $Pa\bar{3}$ structure for $Rb_2CoSi_5O_{12}$ leucite analogue is retained up to 1133 K; above this temperature the sample starts to decompose and then partially melts at 1323 K.

Funding: This research received no external funding.

Data Availability Statement: Not Applicable.

Acknowledgments: The author wishes to acknowledge the use of the EPSRC funded National Chemical Database Service hosted by the Royal Society of Chemistry. The author also wishes to thank Alex Scrimshire of Sheffield Hallam University for the TGA/DSC measurements.

Conflicts of Interest: The author declares no conflict of interest.

References

1. Mazzi, F.; Galli, E.; Gottardi, G. The crystal structure of tetragonal leucite. *Amer. Mineral.* **1976**, *61*, 108–115.
2. Beger, R.M. The crystal structure and chemical composition of pollucite. *Zeits. Krist.* **1969**, *129*, 280–302. https://doi.org/10.1524/zkn. 1969.129.16.280.
3. Sanchez-Valle, C.; Chio, C.-H.; Gatta, G., Single-crystal elastic properties of (Cs,Na)$AlSi_2O_6.H_2O$ pollucite: A zeolite with potential use for long-term storage of Cs radioisotopes. *J. Appl. Phys.* **2010**, *108*, 093509. https://doi.org/10.1063/1.3504613.
4. Bell, A.M.T.; Henderson, C.M.B. Tetragonal-cubic phase transition in $KGaSi_2O_6$ synthetic leucite analogue and its probable mechanism. *J. Solid State Chem.* **2020**, *284*, 121142 https://doi.org/10.1016/j.jssc.2019.121142.
5. Bell, A.M.T.; Henderson, C.M.B. Rietveld Refinement of Dry-Synthesized $Rb_2ZnSi_5O_{12}$ Leucite by Synchrotron X-ray Powder Diffraction. *Acta Cryst.* **1994**, *50*, 984–986.
6. Bell, A.M.T.; Redfern, S.A.T.; Henderson, C.M.B.; Kohn, S.C. Structures of synthetic $K_2MgSi_5O_{12}$ leucites by integrated X-ray powder diffraction, electron diffraction and ^{29}Si MAS NMR methods. *Acta Cryst.* **1994**, *50*, 31–41. https://doi.org/10.1107/SO 108768193008754.
7. Bell, A.M.T.; Henderson, C.M.B. Crystal structures of $K_2[XSi_5O_{12}]$ (X = Fe^{2+}, Co, Zn) and $Rb_2[XSi_5O_{12}]$ (X = Mn) leucites; comparison of monoclinic $P2_1/c$ and *Ia*-3*d* polymorph structures and inverse relationship between tetrahedral cation (T = Si and X)—O bond distances and intertetrahedral T—O—T angles. *Acta Cryst.* **2018**, *74*, 274–286. https://doi.org/10.1107/S2052520618004092.
8. Bell, A.M.T.; Redfern, S.A.T.; Henderson, C.M.B.; Kohn, S.C. Structural relations and tetrahedral ordering pattern of synthetic orthorhombic $Cs_2CdSi_5O_{12}$ leucite: A combined synchrotron X-ray powder diffraction and multinuclear MAS NMR study. *Acta Cryst.* **1994**, *50*, 560–566. https://doi.org/l 0.1 107/SO 108768194003393.
9. Bell, A.M.T.; Henderson, C.M.B. Rietveld refinement of the orthorhombic *Pbca* structures of $Rb_2CdS_5O_{12}$, $Cs_2MnSi_5O_{12}$, $Cs_2CoSi_5O_{12}$ and $Cs_2NiSi_5O_{12}$ leucites by synchrotron X-ray powder diffraction. *Acta Cryst.* **1996**, *52*, 2132–2139. https://doi.org/l 0.1 107/SO 108270196003162.
10. Bell, A.M.T.; Henderson, C.M.B. Crystal structures and cation ordering in $Cs_2MgSi_5O_{12}$, $Rb_2MgSi_5O_{12}$ and $Cs_2ZnSi_5O_{12}$ leucites. *Acta Cryst.* **2009**, *65*, 435–444. https://doi.org/10.1107/SO 108768109024860.
11. Bell, A.M.T.; Knight, K.S.; Henderson, C.M.B.; Fitch, A.N. Revision of the structure of $Cs_2CuSi_5O_{12}$ leucite as orthorhombic Pbca. *Acta Cryst.* **2010**, *66*, 51–59.
12. Bell, A.M.T.; Henderson, C.M.B. Rietveld refinement of the crystal structures of $Rb_2XSi_5O_{12}$ (X = Ni, Mn). *Acta Cryst.* **2016**, *72*, 249–252.
13. Bell, A.M.T.; Henderson, C.M.B. A study of possible extra-framework cation ordering in *Pbca* leucite structures with stoichiometry $RbCsXSi_5O_{12}$ (X = Mg, Ni, Cd). *Powder Diffr.* **2019**, *34*, S2–S7. https://doi.org/10.1017/S0885715619000071.
14. Kohn, S.C.; Henderson, C.M.B.; Dupree, R. NMR Studies of the Leucite Analogues $X_2YSi_5O_{12}$, where X = K, Rb, Cs; Y = Mg, Zn, Cd. *Phys Chem Miner.* **1994**, *21*, 176–190.
15. Palmer, D.C.; Dove, M.T.; Ibberson, R.M.; Powell, B.M. Structural behavior, crystal chemistry, and phase transitions in substituted leucite: High-resolution neutron powder diffraction studies. *Amer. Mineral.* **1997**, *82*, 16–29.
16. Redfern, S.A.T.; Henderson, C.M.B. Monoclinic-orthorhombic phase transition in the $K_2MgSi_5O_{12}$ leucite analog. *Amer. Mineral.* **1996**, *81*, 369–374.
17. Bell, A.M.T.; Clegg, F.; Henderson, C.M.B. Monoclinic-orthorhombic first-order phase transition in $K_2ZnSi_5O_{12}$ leucite analogue; transition mechanism and spontaneous strain analysis. *Mineral. Mag.* **2021**, *85*, 752–771. https://doi.org/10.1180/mgm.2021.67.
18. Bell, A.M.T.; Henderson, C.M.B. High-temperature synchrotron X-ray powder diffraction study of $Cs_2XSi_5O_{12}$ (X = Cd, Cu, Zn) leucites. *Mineral. Mag.* **2012**, *76*, 1257–1280. https://doi.org/10.1180/minmag.2012.076.5.12.
19. Torres-Martinez, L.M.; West, A.R. Pollucite- and leucite-related phases: $A_2BX_5O_{12}$ and ACX_2O_6 (A = K, Rb, Cs; B = Be, Mg, Fe, Co, Ni, Zn, Cd; C = B, Al, Ga, Fe, Cr; X = Si, Ge). *Zeits. Anorg. Allg. Chem.* **1989**, *573*, 223–230. https://doi.org/10.1002/zaac. 19895730123.
20. Rietveld, H.M. A profile refinement method for nuclear and magnetic structures. *J. Appl. Cryst.* **1969**, *2*, 65–71. https://doi.org/10.1107/S0021889869006558.
21. Toby, B.H.; Von Dreele, R.B. *GSAS-II*: The genesis of a modern open-source all purpose crystallography software package. *J. Appl. Cryst.* **2013**, *46*, 544–549. https://doi.org/10.1107/S0021889813003531.
22. Momma, K.; Izumi, F. VESTA 3 for three-dimensional visualization of crystal, volumetric and morphology data. *J. Appl. Cryst.* **2011**, *44*, 1272–1276. https://doi.org/10.1107/S0021889811038970.
23. Sasaki, S.; Fujino, K.; Takeuchi, Y. X-ray determination of electron-density distributions in oxides, Mg O, Mn O, Co O, and Ni O, and atomic scattering factors of their constituent atoms. *Proc. Jpn. Acad.* **1979**, *55*, 43–48. https://doi.org/10.2183/pjab.55.43.

24. Taylor, D. Thermal Expansion Data: I. Binary Oxides with the Sodium Chloride and Wurtzite Structures, MO. *Trans. J. Br. Ceram. Soc.* **1984**, *83*, 5–9.
25. Robinson, K.; Gibbs, G.V.; Ribbe, P.H. Quadratic Elongation: A Quantitative Measure of Distortion in Coordination Polyhedra. *Science* **1971**, *172*, 567–570.
26. Azuma, M.; Chen, W.; Seki, H.; Czapski, M.; Olga, S.; Oka, K.; Mizumaki, M.; Watanuki, T.; Ishimatsu, N.; Kawamura, N.; et al. Colossal negative thermal expansion in $BiNiO_3$ induced by intermetallic charge transfer. *Nat. Commun.* **2011**, *2*, 347. https://doi.org/10.1038/ncomms1361.
27. Diop, L.V.B.; Isnard, O.; Amara, M.; Gay, F.; Itié, J.P. Giant negative thermal expansion across the first-order magnetoelastic transition in $Hf_{0.86}Ta_{0.14}Fe_2$. *J. Alloys Compd.* **2020**, *845*, 156310. https://doi.org/10.1016/j.jallcom.2020.156310. hal-02918967.
28. Taylor, D.; Henderson, C.M.B. The thermal expansion of the leucite group of minerals. *Am. Mineral.* **1968**, *53*, 1476–1489.